Technical aspects of fast magic-angle turning NMR for dilute spin-1/2 nuclei with broad spectra

Y.-Y. Hu, K. Schmidt-Rohr*

Ames Laboratory and Department of Chemistry, Iowa State University, Ames, IA 50011, USA

ARTICLE INFO

ABSTRACT

For obtaining sideband-free spectra of high-Z spin-1/2 nuclei with large (> 1000 ppm) chemical-shift anisotropies and broad isotropic-shift dispersion, we recently identified Gan's modified five-pulse magic-angle turning (MAT) experiment as the best available broadband pulse sequence, and adapted it to fast magic-angle spinning. Here, we discuss technical aspects such as pulse timings that compensate for off-resonance effects and are suitable for large CSAs over a range of $1.8\gamma B_1$; methods to minimize the duration of z-periods by cyclic decrementation; shearing without digitization artifacts, by sharing between channels (points); and maximizing the sensitivity by echo-matched full-Gaussian filtering. The method is demonstrated on a model sample of mixed amino acids and its large bandwidth is highlighted by comparison with the multiple-π-pulse PASS technique. Applications to various tellurides are shown; these include GeTe, Sb_2Te_3 and $Ag_{0.53}Pb_{18}Sb_{1.2}Te_{20}$, with spectra spanning up to 190 kHz, at 22 kHz MAS. We have also determined the ^{125}Te chemical shift anisotropies from the intensities of the spinning sidebands resolved by isotropic-shift separation.

© 2011 Published by Elsevier Inc.

1. Introduction

Magic-angle spinning NMR spectra of high-Z nuclei such as ^{125}Te, ^{207}Pb, ^{119}Sn, and ^{113}Cd in non-cubic environments are often crowded with spinning sidebands overlapped with the peaks at the isotropic shifts over a broad spectral range; this overlap interferes with the determination of isotropic chemical and Knight shifts, and evaluation of chemical shift anisotropies. Most methods designed for suppressing sidebands [1,2] employ long pulses and cannot achieve broadband excitation, leaving severely distorted spectra for spin systems of large spectral range. Magic angle turning experiments [3–5] that employ only short pulses are promising for achieving excitation over a broad spectral range. Recently, we adapted Gan's MAT$^\pm$ experiment [6] to fast magic angle spinning with frequencies > 20 kHz, hereafter referred to as fast MAT [7], to maximize the sensitivity by solving pulse timing issues due to finite pulses and short rotation periods. Fast MAT is presently the best broadband method to separate isotropic chemical shift and chemical shift anisotropy. It has been successfully applied to various tellurides with spectral ranges up to $\sim 1.8\gamma B_1$ without significant spectral distortions [7].

In this paper, we detail technical aspects of the fast MAT experiment, including analysis and quantitative numerical simulations of the nearly linear off-resonance phase shift, which can be considered as precession during the finite pulses and can therefore be included as an effective evolution time, and cyclic decrementation of the z-periods designed to keep them short in order to avoid T_1 relaxation or possible spin diffusion without the loss of required synchronization. For data processing, we have employed echo-matched full Gaussian time-domain filtering to improve the signal-to-noise ratio, taking advantage of moving echoes (when $t_2 = t_1$) due to the refocusing of the isotropic chemical shifts. We have also applied the sharing-between-channels approach [8] after shearing to avoid spectral artifacts associated with digital rounding when shearing parameters are not integers.

In addition, PASS [2,9,10] and fast MAT are compared in terms of sensitivity, spectral distortions, and experimental implementation under similar conditions on a model sample. For relatively narrow spectra, PASS is preferable due to its better sensitivity, and simpler experimental set-up and data processing. However, for spectra whose width exceeds the pulse nutation frequency, the superiority of fast MAT in producing sideband-free spectra without significant spectral distortions is demonstrated.

2. Experimental

2.1. Samples

A mixture of seven amino acids with different ^{13}C labeling sites, including 1-^{13}C-Leu, 1-^{13}C-Gly, 2-^{13}C-Leu, 2-^{13}C-Gly, 3-^{13}C-Ala, 1-^{13}C-Ala, and 1-^{13}C-N$_\alpha$-(tert-butoxycarbonyl)-L-arginine, were

used as a model sample. All of the labeled amino acids were purchased from CIL Inc. GeTe was used as received from GFS chemicals. Samples of $Ag_{0.53}Pb_{18}Sb_{1.2}Te_{20}$ and Sb_2Te_3 have been described in Ref. [11].

2.2. NMR parameters

All of the ^{125}Te NMR experiments were performed using a Bruker DSX400 spectrometer at 126 MHz for ^{125}Te. A 2.5-mm MAS probe head was used at a spinning speed of 21.74 kHz (synchronized with t_1 increments) with ^{125}Te 90° pulse length of 2.4 μs. All the fast MAT ^{125}Te spectra were obtained with the first five pulses of 2 μs and the last pulse of 3.5 μs in order to achieve broad excitation. EXORCYCLE phase cycling [12] was used for pulse length error compensation for the last pulse. Recycle delays of 150 ms for $Ag_{0.53}Pb_{18}Sb_{1.2}Te_{20}$, 50 ms for Sb_2Te_3, and 50 ms for GeTe were used. In the S^- MAT datasets, the number of t_1 increments was 400 for $Ag_{0.53}Pb_{18}Sb_{1.2}Te_{20}$, 280 for Sb_2Te_3, and 320 for GeTe, while in the S^+ MAT datasets, the number of t_1 increments was reduced to 80 for $Ag_{0.53}Pb_{18}Sb_{1.2}Te_{20}$, 40 for Sb_2Te_3, and 40 for GeTe. The ^{125}Te chemical shift relative to $Te(OH)_6$ in solution was calibrated using TeO_2 at $+750$ ppm as a secondary reference [13].

For all ^{13}C NMR experiments on the model compounds, a 4-mm double resonance MAS probe head was used at a spinning speed of ca. 3 kHz. Weak ^{13}C 22-μs 90° pulses were purposely applied to test off-resonance tolerance of fast MAT and PASS. Reference spectra using fast MAT and 5-pulse PASS were obtained with strong 4.4-μs 90° pulses.

3. Theoretical background and experimental setup

3.1. Gan's MAT experiment

Fig. 1 shows the basic pulse sequence used for MAT with a minimum number of pulses. Two evolution periods of duration $t_{1,nom}/2$ are each followed by a z-storage period that allows the rotor to reach a suitable orientation before evolution of transverse magnetization is resumed. Gan's modified MAT experiment, MAT$^{\pm}$ [6], achieves absorptive line shapes by using two slightly different versions of the pulse sequence. One of them is identical to the original MAT [3] with $t_{zA} = t_{zB} = t_r/3 - t_1/2$, generating the MAT$^+$ dataset by combining signals for suitably chosen pulse phases [3]

$$S^+(t_1,t_2) = \left\langle \sum_{n=-\infty}^{\infty} S_n \exp\{i(\omega_{iso}-n\omega_r/2)t_1\}\exp\{i(\omega_{iso}+n\omega_r)t_2\}R \right\rangle,$$
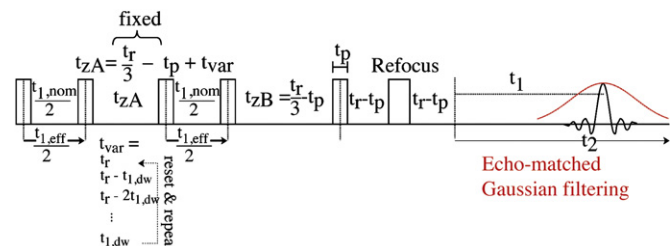(1a)

Fig. 1. Broadband fast MAT pulse sequence for obtaining pure isotropic-shift spectra and sideband separation. The unequal timings of the z-periods shown are for the "t_1 time-reversed" MAT$^-$ dataset, while the MAT$^+$ dataset is obtained with $t_{zB} = t_{zA}$, both decremented with increasing $t_{1,nom}/2$, illustrated by t_{var} values taken from the delay list, as shown at the bottom of the figure. Flip angles can be 60°–90° for the first five pulses of duration t_p, and 120°–180° for the last pulse. The pulse program is available from our website (http://www.public.iastate.edu/~nmrksr/). Echo-matched Gaussian filtering applied to the time domain signal to optimize the sensitivity is indicated schematically. For $t_{1,eff}/2 = 0$, a simplified pulse sequence with only the last two pulses is used (see text).

where t_r is the rotor period, S_n is the intensity of the nth order spinning sideband, and R accounts for relaxation effects. The other pulse sequence differs from the original one by an additional delay of $t_1/2$ before the last read-out 90° pulse, producing the "time-reversed" MAT$^-$ dataset

$$S^-(t_1,t_2) = \left\langle \sum_{n=-\infty}^{\infty} S_n \exp\{-i(\omega_{iso}-n\omega_r/2)t_1\}\exp\{i(\omega_{iso}+n\omega_r)t_2\}R \right\rangle.$$
(1b)

The sum and difference of these two datasets create cosine- and sine-modulated 2D datasets, respectively, which can be Fourier transformed to yield purely absorptive 2D spectra. After spectral shearing, 2D spectra with an "infinite-speed" isotropic-shift projection along ω_1 and anisotropic powder pattern or sidebands along ω_2 are produced.

Gan's original MAT experiments were performed at slow spinning speeds for narrow spectral ranges (< 20 kHz), while for our purpose, spinning speeds greater than 20 kHz are necessary to maximize the sensitivity and cover the spectral ranges larger than 100 kHz needed due to wide chemical shift dispersion. Broadband spectra produce large phase shifts that can be explained as resulting from the evolution during pulses of finite duration. These lead to artifacts which can be corrected for as described below. Also, the rotor period t_r becomes short at fast spinning and the t_1 evolution time has to exceed one t_r to attain reasonable resolution, rather than $t_1 < t_r$ at spinning speeds on the order of hundreds of hertz. Therefore, modifications of the durations of the z-periods (t_{zA} and t_{zB}) are necessary to maintain pulse synchronization as well as avoid T_1 relaxation and potential spin diffusion. Moreover, regular data processing procedures can be refined by employing echo-matched full Gaussian filtering to maximize the sensitivity and sharing between channels [8] after spectral shearing to eliminate spectral artifacts resulting from digital rounding with traditional shearing procedures.

3.2. Simulation of pulse excitation effects in fast MAT

In fast MAT experiments [7], four $\sim90^{\circ}$ pulses are used in addition to the regular excitation and Hahn-echo pulse. Here, we analyze the effect of the pulses on magnetization off-resonance and show that the resulting phase shift, which is nearly linear with off-resonance frequency $\Delta\omega$, can be considered as precession during the pulses and thus compensated for.

The bandwidth of a single 90° x-pulse applied to z-magnetization is $2\gamma B_1$ if the full width at half maximum of the profile of the y-magnetization as a function of $\Delta\omega$ is considered [14]. However, the profile of the total transverse magnetization vs. $\Delta\omega$ is significantly wider, $> 5\gamma B_1$ [15]. The difference arises from a nearly linear off-resonance phase shift $\sim\Delta\omega t_p/2$ [15] of the transverse magnetization.

The MAT sequence contains two pairs of $\sim90^{\circ}$ pulses, with the first flipping z-magnetization to the transverse plane and the second restoring one magnetization component to z. It is instructive to start by considering one pair of ideal δ-pulses. The transverse magnetization generated by the first x-pulse precesses as

$$M_y = M_0 \cos\Delta\omega t_1,$$
(2a)

$$M_x = M_0 \sin\Delta\omega t_1.$$
(2b)

By the second pulse of suitable phase, either component can be stored along the z-direction

$$M_{z,cos} = M_0 \cos\Delta\omega t_1,$$
(2c)

$$M_{z,sin} = M_0 \sin\Delta\omega t_1.$$
(2d)

The ratio of these two components can be written in terms of the evolution phase

$$\phi = \Delta\omega t_1, \tag{3a}$$

$$\tan(\phi) = M_{z,\sin}/M_{z,\cos}. \tag{3b}$$

This relation will allow us to determine the effective duration of precession during pulses of finite length (Fig. 2a).

We have analyzed the excitation effect by numerically simulating the spin evolution during a back-to-back pulse pair (without any delay, nominal $t_{1,nom}=0$) as a function of off-resonance frequency $\Delta\omega$. The effective magnetic field in the rotating frame is calculated as $\overrightarrow{B_{eff}} = \overrightarrow{B_1} + \overrightarrow{\Delta B_0}$, where $\Delta\omega = -\gamma|\overrightarrow{\Delta B_0}|$. The second pulse is phase cycled along $\pm y$ and $\pm x$ to obtain the cosine and sine components $M_{\cos}$ and $M_{\sin}$ of the magnetization, respectively. The $\pm$ alternation of the pulse phase, combined with the corresponding alternation of the receiver phase, removes signal from residual transverse magnetization and distortions that arise for flip angles $\neq 90°$. For each pulse, the precession of the magnetization around the effective magnetic field by an angle $\chi = \omega_{eff}t_p$ with $\omega_{eff} = -\gamma|\overrightarrow{B_{eff}}|$ is calculated using the rotation matrix $R_{\beta\alpha}(\chi) = \tilde{R}(0,-\beta,-\alpha)\tilde{R}(\alpha,\beta,-\chi)$ [14], where α and β are the polar coordinates of the effective field ($\alpha=0°$ for an x-, and $\alpha=90°$ for a y-pulse, and $\beta=90°$ for both) and $\tilde{R}$ is the standard active rotation matrix for the three Euler angles defining the rotation. The magnetization vector after the rotation is $\overrightarrow{M_{after}} = R_{\beta\alpha}(\chi)\overrightarrow{M_{before}}$. The initial magnetization is along the z-axis, $\overrightarrow{M_0} = (0,0,1)^T$. After pulse phase cycling as described above, the z-magnetization components $M_{z,\sin}$ and $M_{z,\cos}$ are calculated as a function of $\Delta\omega$, in a range of $\pm 4\omega_1$ where $\omega_1 = -\gamma B_1$. The length of the effective transverse magnetization during the pulses (M_{transv}) is obtained as

$$M_{transv} = \sqrt{M_{z,\sin}^2 + M_{z,\cos}^2}, \tag{4a}$$

while the effective evolution phase ϕ_0 during the pulses can be defined analogous to Eq. (3) above

$$\tan(\phi_0) = M_{z,\sin}/M_{z,\cos}. \tag{4b}$$

Fig. 2b shows that pulses with smaller flip angles give broader excitation profiles than long pulses, as expected. Therefore, NMR methods aiming at achieving broadband excitation should employ short pulses; however, there is usually a trade-off in terms of reduced sensitivity. Fig. 2c displays a plot of ϕ_0/ϕ_P,
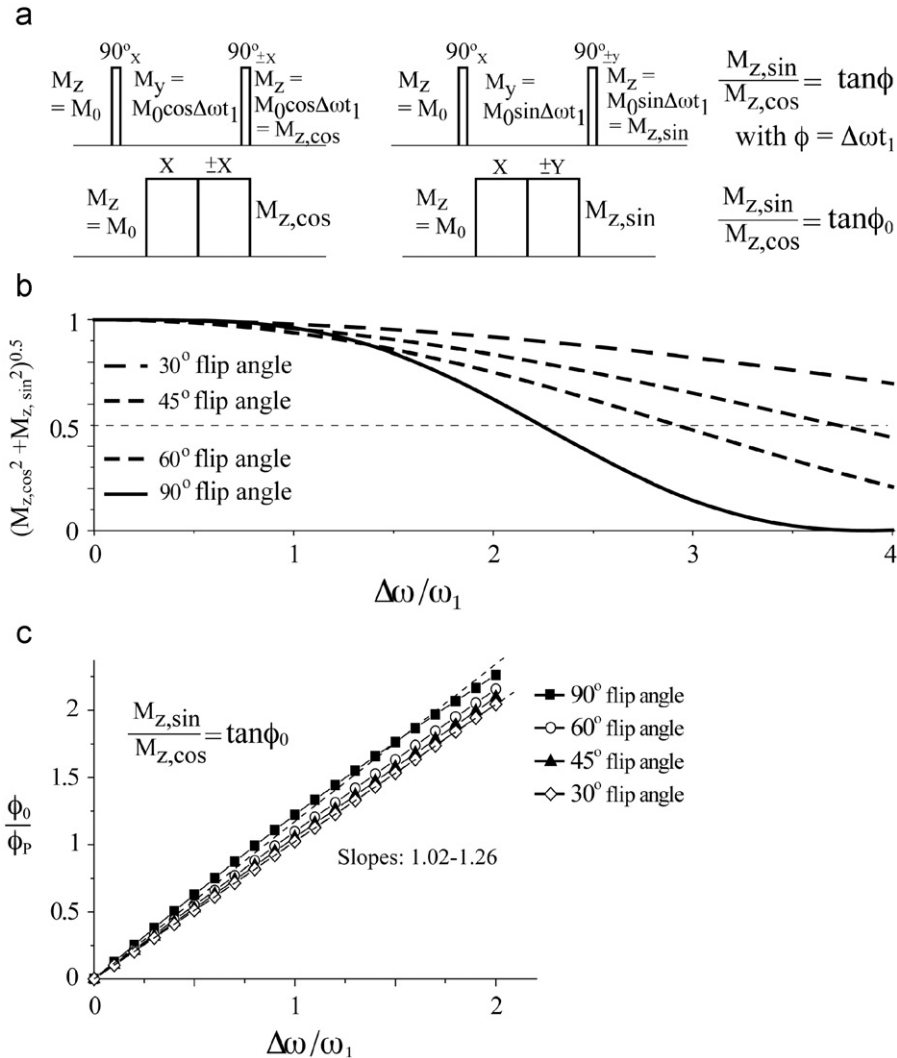

Fig. 2. Simulation of pulse excitation profiles and effects. (a) Pairs of δ-pulses (top) are compared with pairs of back-to-back pulses of finite length t_p (bottom), in terms of evolution of transverse magnetization between or during the pulses, giving rise to an evolution phase ϕ and ϕ_0, respectively. Pulse pairs generating cosine and sine modulation are shown for each case. (b) "Magnitude" excitation profiles of a pair of back-to-back pulses with 30°–90° flip angles, as a function of the offset $\Delta\omega$ normalized by $\omega_1 = -\gamma B_1$. (c) Numerical simulation results of ϕ_0/ϕ_P (with the nominal pulse flip angle $\phi_P = \omega_1 t_p$) vs. $\Delta\omega/\omega_1$ for a pair of back-to-back pulses of 30°–90° flip angles.

i.e., the effective evolution phase normalized by the nominal pulse flip angle $\phi_P = \omega_1 t_p$, vs. $\Delta\omega/\omega_1$. The phase shift ϕ_0/ϕ_P is seen to grow linearly with $\Delta\omega/\omega_1$, with a slope $s \approx 1$ for small flip angles and $s = 1.26$ for $90°$ pulses. Therefore, after a pair of consecutive $90°$ pulses, the effective evolution phase is

$$\phi_0 = s(\Delta\omega/\omega_1)\phi_P = \Delta\omega s t_p. \tag{5}$$

For a finite nominal evolution time $t_{1,nom}/2$,

$$\phi = \Delta\omega t_{1,eff}/2 = \phi_0 + \Delta\omega t_{1,nom}/2 = \Delta\omega(t_{1,nom}/2 + s t_p), \tag{6}$$

which means that the $t_{1,nom}/2 = 0$ slice of MAT corresponds to an effective evolution time $t_{1,eff}/2 = s t_p$. This results in a large distortion of the spectrum for nominal $t_{1,nom}/2 = 0$. It can be partially removed by linear phase correction, but that requires time-consuming determination of the large correction phase and leaves residual baseline artifacts. To avoid this problem, we choose the increment of $t_1/2$ as $t_{1,dw} = s t_p$, so that the phase of Eq. (6) for nominal $t_{1,nom}/2 = 0$ equals effective $t_{1,eff}/2 = t_{1,dw} = s t_p$ ("second t_1-slice"). The signal for effective $t_{1,eff}/2 = 0$ is then approximated by separately recording the signal without the two pairs of storage and read-out pulses. Processing of the $t_{1,eff}/2 = 0$ signal also enables determination of the optimum pre-detection delay and phase correction parameters in ω_2. Later, the $t_{1,eff}/2 = 0$ slice is incorporated into both the S^+ and S^- 2D spectra as the first slice in ω_1. If the intensity of this "first slice" is somewhat too high compared to the rest because of pulse flip angles deviating from $90°$, characteristic ridges are seen in the 2D spectrum parallel to the ω_1 axis. These simple, distinctive artifacts can be eliminated by reducing the amplitude of the first slice by $(1 - \cos(2\phi_P))^2/4$, in addition to a factor of $1/4$ that takes into account that four scans with different excitation and storage pulses must be added to generate the signal in Eq. (1a) or (1b). In our experiments using four $90°$ pulses, nearly ideal weighting factors of 0.9–1 gave good results.

3.3. Cyclic decrementation of z-periods

The time between the start of the two evolution periods must be $n t_r + 2\pi/3$ in MAT. Given that the first part of this time is the evolution period $t_1/2$, the delay t_{zA} between the end of the first and beginning of the next evolution period must be $t_{zA} = n t_r + 2\pi/3 - t_1/2$. The rotation period t_r is short at fast spinning and t_z has to remain non-negative. Rather than starting with a fixed long $n t_r$, which could result in spin exchange, T_1 relaxation or de-synchronization of the rotation and the pulse sequence, we use a cyclic delay list to minimize the length of the z-periods while preserving the necessary synchronization. For this purpose, the inter-pulse delay (t_{zA}) is split into two parts $t_{zA} = (t_r/3) + N t_r + t_{var}$ (see Fig. 1). One delay is fixed and equal to $t_r/3$ minus the time needed for the intervening pulses, plus a couple of rotation periods for relaxation of transverse magnetization. The other delay, t_{var}, is varied and taken from a list with $n = t_r/t_{1,dw}$ entries (see bottom of Fig. 1), where $t_{1,dw}$ is the dwell time of $t_1/2$ and t_r is chosen as an integer multiple of $t_{1,dw}$. The value of t_{var} starts out with a value of t_r for $t_1 = 0$ and is decremented in steps of $t_{1,dw}$. After t_{var} has reached $t_{1,dw}$ in the cyclic list, it jumps back to t_r for $t_1/2 = n t_r$. For example, with $t_{1,dw} = 2$ μs and $t_r = 46$ μs, the list is {46, 44, 42, …, 6, 4, and 2 μs}. Since the delays are short, active synchronization of the pulse timing with the rotor phase is not necessary.

3.4. Echoes and optimized filtering

For our purposes, dead-time free detection using a Hahn echo in fast MAT is indispensable, given that the time constants T_2^* of the FIDs are ~ 3 μs, if the line widths are ~ 100 kHz.

In MAT$^\pm$ experiments with powder averaging, Eq. (1) can be rearranged and written as

$$S^+(t_1, t_2) = \left\langle \sum_{n=-\infty}^{\infty} S_n \exp\{i\omega_{iso}(t_1 + t_2)\}\exp\{in\omega_r(-t_1/2 + t_2)R\right\rangle, \tag{7a}$$

$$S^-(t_1, t_2) = \left\langle \sum_{n=-\infty}^{\infty} S_n \exp\{i\omega_{iso}(-t_1 + t_2)\}\exp\{in\omega_r(t_1/2 + t_2)\}R\right\rangle. \tag{7b}$$

In Gan's MAT$^\pm$ experiments with a spinning frequency of ~ 100 Hz, echoes are observed at $t_2 = t_1/2$ in the S^+ dataset due to refocusing of the CSA. Rotational echoes occur at longer t_2. In fast MAT experiments, the sideband intensities are reduced by the fast spinning. Therefore, no significant echoes from CSA refocusing are detected, for instance, in the fast MAT experiments on the mixed amino acids.

However, given a broad distribution of isotropic chemical shifts ω_{iso} (i.e., chemical shift dispersion), the signal forms pronounced echoes at $t_2 = t_1$ in the S^- dataset due to refocusing of isotropic chemical shifts in fast MAT. The echo dominates the observable signal, producing sharp ridges in the spectra (seen in Figs. 4 and 5a). Outside of the echo region, $t_1 - 4T_2^* < t_2 < t_1 + 4T_2^*$, noise dominates the observed time-domain signal. Therefore, the S/N ratio of the spectrum can be improved by multiplying the time signal for each t_1 value with a Gaussian function whose maximum is shifted to match the position of the echo maximum, as in full-echo detection schemes [16]. The S/N ratio has been improved significantly by this matched filtering for all the telluride samples studied, as shown below.

In contrast, the S^+ dataset contains only an anti-echo term, $\langle \exp(i\omega_{iso}(t_1 + t_2))\rangle$. As a result, for $t_1 > 2T_2^*$, the intensity is negligible ($<2\%$) and does not need to be recorded, which provides a significant reduction in measuring time.

3.5. Spectral shearing in 2D fast MAT

The 2D spectra obtained directly from fast MAT contain tilted straight ridges (Figs. 3a and 4a) since according to Eq. (7), both dimensions contain a mixture of isotropic chemical shifts and CSA [3]. Therefore, shearing is necessary to achieve a spectrum with peaks only at the isotropic shifts in the ω_1 dimension and sidebands in the ω_2 dimension for convenient data analysis.

Spectral shearing along ω_1 has been achieved in experiments such as MQMAS [17] and DAS [16] by applying a t_1-proportional first-order linear phase correction after Fourier transformation in ω_2. However, in this paper, spectral shearing was performed in both dimensions, and the second shearing step must be applied in the spectral domain. Signals appear at $(\omega_{iso} - \omega_{aniso}/2, \omega_{iso} + \omega_{aniso})$, and the first shearing step, along ω_1, gives

$$\omega_1'' = \omega_1 + 1/2\omega_2 = (\omega_{iso} - \omega_{aniso}/2) + 1/2(\omega_{iso} + \omega_{aniso}) = 3/2\omega_{iso}. \tag{8a}$$

This is scaled by $2/3$ to provide the isotropic chemical shift in ω_1

$$\omega_1' = 2/3\omega_1'' = \omega_{iso}. \tag{8b}$$

The second shearing step, along ω_2, yields the pure anisotropic frequency under MAS

$$\omega_2' = \omega_2 - \omega_1' = (\omega_{iso} + \omega_{aniso}) - \omega_{iso} = \omega_{aniso}. \tag{8c}$$

The shearing procedure is demonstrated on the fast MAT 2D spectra of the model sample of mixed amino acids (Fig. 3) and of Sb$_2$Te$_3$ (Fig. 4). For technical reasons, the scaling in the vertical dimension by $2/3$ was done at the very start. As seen in Fig. 3, after shearing along ω_1, $\omega_1' = 2/3\omega_1 + 1/3\omega_2 = 2(\omega_{iso} - \omega_{aniso}/2)/3 + 1/3(\omega_{iso} + \omega_{aniso}) = \omega_{iso}$, the sidebands have been removed from
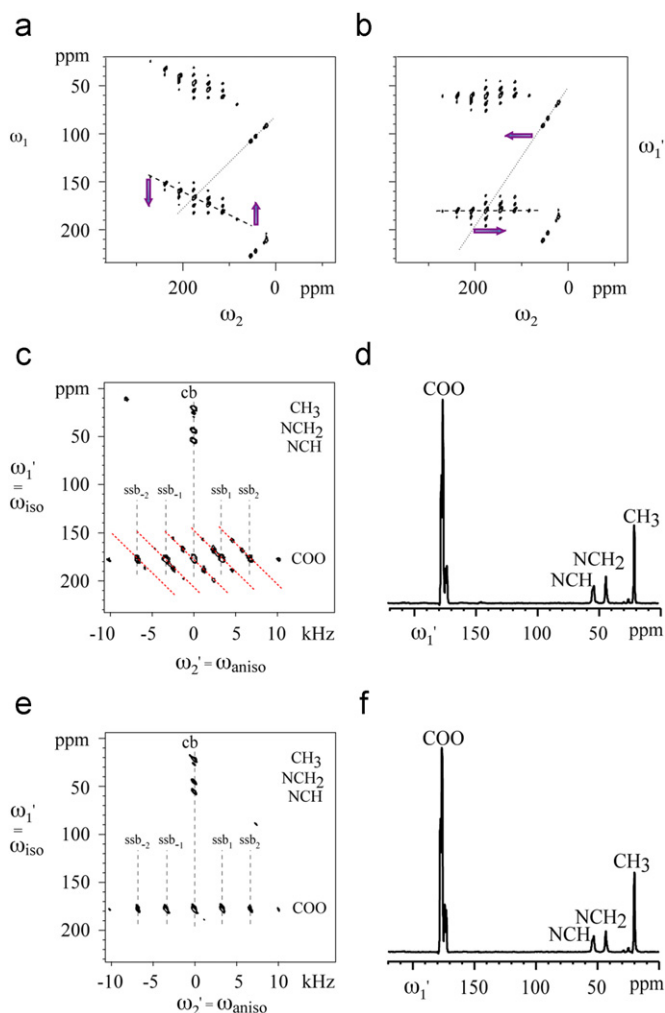
Fig. 3. Fast MAT spectra of a mixture of seven ^{13}C-labeled amino acids ($1-^{13}$C-Leu, $1-^{13}$C-Gly, $2-^{13}$C-Leu, $2-^{13}$C-Gly, $3-^{13}$C-Ala, and $1-^{13}$C-Ala, $1-^{13}$C-N$_\alpha$-(tert-butoxycarbonyl)-L-arginine) acquired with weak long pulses of $\gamma B_1/2\pi = 11.4$ kHz. (a) 2D fast MAT spectrum before shearing. The chemical shift was scaled by a factor of 2/3 in the ω_1 dimension. Each peak is replicated and shifted by ω_r in ω_1 by inserting zero-slices alternating with measured data in t_1. (b) After shearing along ω_1. (c) After shearing along ω_2. Only the central region of the spectrum in ω_2' is shown, eliminating the replicated signals. Sideband artifacts (marked by slanted red lines), which are due to the long (22 μs) pulse lengths, do not produce significant artifacts in the vertical slices for the various sideband orders (marked by dashed lines). (d) 1D spectrum of pure isotropic chemical shifts from the sum of centerband and sidebands generated from projections of the sheared fast MAT 2D spectrum in (c). (e) Same as (d), but with strong short pulses ($\gamma B_1/2\pi = 57$ kHz), for reference. (f) 1D spectrum of pure isotropic chemical shifts from the sum of centerband and sidebands generated from projections of the sheared fast MAT 2D spectrum in (e). (For interpretation of the references to color in this figure legend, the reader is referred to the web version of this article.)

the ω_1 dimension (see Fig. 3b). Subsequent shearing along ω_2 yields a spectrum with isotropic chemical shifts along the ω_1' dimension and sidebands along ω_2' (Fig. 3c).

After shearing (Fig. 4c), the ^{125}Te signals in the fast MAT 2D spectrum of Sb$_2$Te$_3$ are concentrated in vertical ridges. The cross sections along ω_2 provide sideband patterns, and the analysis of their intensities can provide information on the chemical shift anisotropy associated with the selected isotropic shift in ω_1'.

3.6. Sharing between channels after spectral shearing

Commonly, shearing is achieved by shifting columns or rows of the 2D matrix by a number of points m that increases linearly with the distance of the column or row number n from the center

of the spectrum. In other words

$$m(n) = \text{tiltfactor} \times (N/2 - n),$$

where N is the total number of columns or rows, and tiltfactor controls the shearing angle. In most cases, $m(n)$ is not an integer and default digital rounding will cause inaccurate shearing and discontinuous profiles ("steps") in the sheared spectra. This problem can be circumvented by applying a sharing-between-channels approach [8] in off-line data processing: the intensity of the matrix element that needs to be shifted is shared between two adjacent channels (points) $(n+\text{floor}(m))$ and $(n+\text{floor}(m)+1)$ in a row or column, with linear weighting factors of (floor $(m+1)-m$) and $(m-\text{floor}(m))$, respectively; here, floor(m) is the nearest integer smaller than m. For example, if $m=3.1$, channel $n+3$ is given 90% of the intensity, and channel $n+4$, 10%.

3.7. Doubling of 2D fast MAT spectra in ω_1

Since the isotropic shifts of interest in our research span a wide range, shearing in the ω_1 dimension can result in aliasing of off-resonance spectral regions. Although the spectra can be reconstructed to correct for aliasing, a simpler way is to replicate the spectra in the ω_1 dimension by inserting pairs of slices with zero intensity into the t_1 time data so that they alternate with pairs of measured data slices [18].

3.8. Sideband artifacts

Due to pulse imperfections, in particular finite pulse length, the fast MAT 2D spectra can exhibit sideband artifacts, mostly at $\pm \omega_r$ from the expected bands, in both spectral dimensions. This may be explained in terms of partial desynchronization of evolution and detection due to the long duration of the pulses. The transverse magnetization components generated at the beginning and at the end of a pulse start their evolutions at different rotor orientations. As a result, the anisotropic-frequency evolution is different from that for the ideal δ-pulse. The iso-tropic-shift evolution is not affected, so the signals must show up at $\omega_{iso}+n\omega_r$ in ω_2 and $\omega_{iso}-n'/2\omega_r$ in ω_1. The extreme case of complete desynchronization of evolution and detection is easy to treat, since this factorizes the sideband patterns in the two dimensions, e.g.

$$S^+(t_1,t_2) = \left\langle \sum_{n'=-\infty}^{\infty} S_{n'} \exp\{i(\omega_{iso}-n'\omega_r/2)t_1\}R_1 \right\rangle$$
$$\times \left\langle \sum_{n=-\infty}^{\infty} S_n \exp\{i(\omega_{iso}+n\omega_r)t_2\}R_2 \right\rangle, \quad (9)$$

and the corresponding spectrum would show intensity at all possible sideband positions (n', n) in the 2D plane. The only slight desynchronization due to finite pulse lengths results mostly in next-neighbor sidebands $(n\pm 1, n)$ and $(n, n\pm 1)$.

Fortunately, these "first-order" sideband artifacts do not produce signal in the slices containing the real center- and sideband peaks, due to the slope of $-1/3$ of the sideband line (see dotted lines in Fig. 3c). Only third-order sideband artifacts coincide with signal slices, and these higher-order sidebands are negligibly small even for long pulses. Fast MAT 2D spectra with short strong pulses shown in Fig. 3e do not exhibit any sideband artifacts. The isotropic spectra obtained from the fast MAT with long weak pulses (Fig. 3e) and short strong pulses (Fig. 3f) match each other, which indicates that the sideband artifacts do not produce visible distortions in the 1D "infinite-speed" spectra of interest.
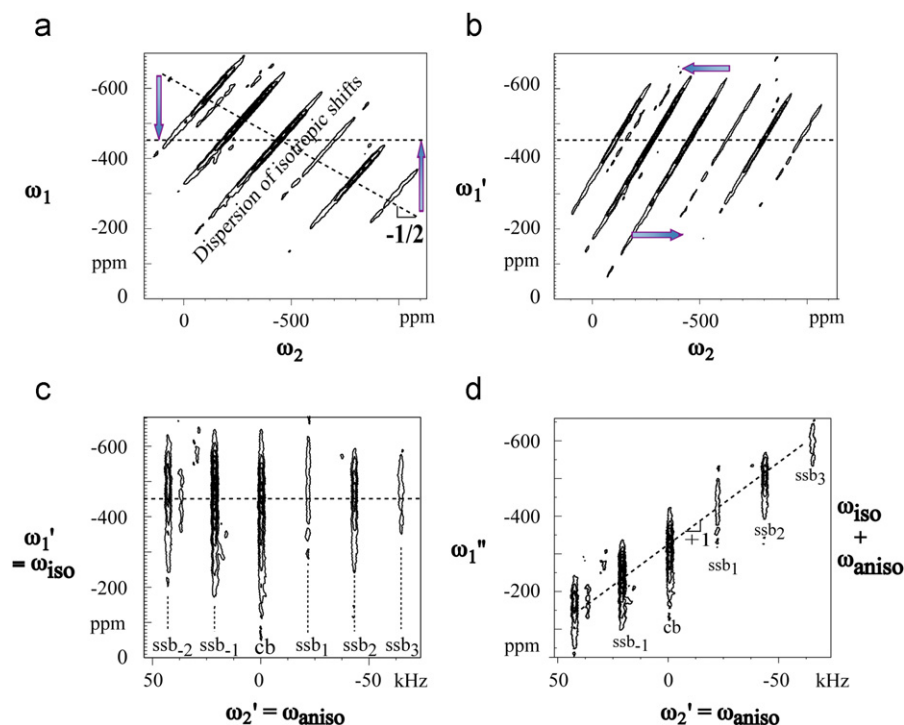
Fig. 4. Shearing of a fast MAT spectrum of Sb_2Te_3. (a) Original 2D fast MAT spectrum before shearing. The chemical shift was scaled by a factor of 2/3 in the ω_1 dimension. (b) After shearing along ω_1 by $\arctan(-1/2)=-26.6°$. (c) After further shearing along ω_2 by $\arctan(-2/3)=-33°$. Pure isotropic chemical shift along ω_1' and sidebands along ω_2' are obtained. (d) After further shearing along ω_1' by $\arctan(1)=45°$ to achieve $\omega_1''=\omega_1'+\omega_2'=\omega_{iso}+\omega_{aniso}$ for the purpose of a "quality test" and deconvolution of the regular MAS spectrum into subspectra of sideband order n.
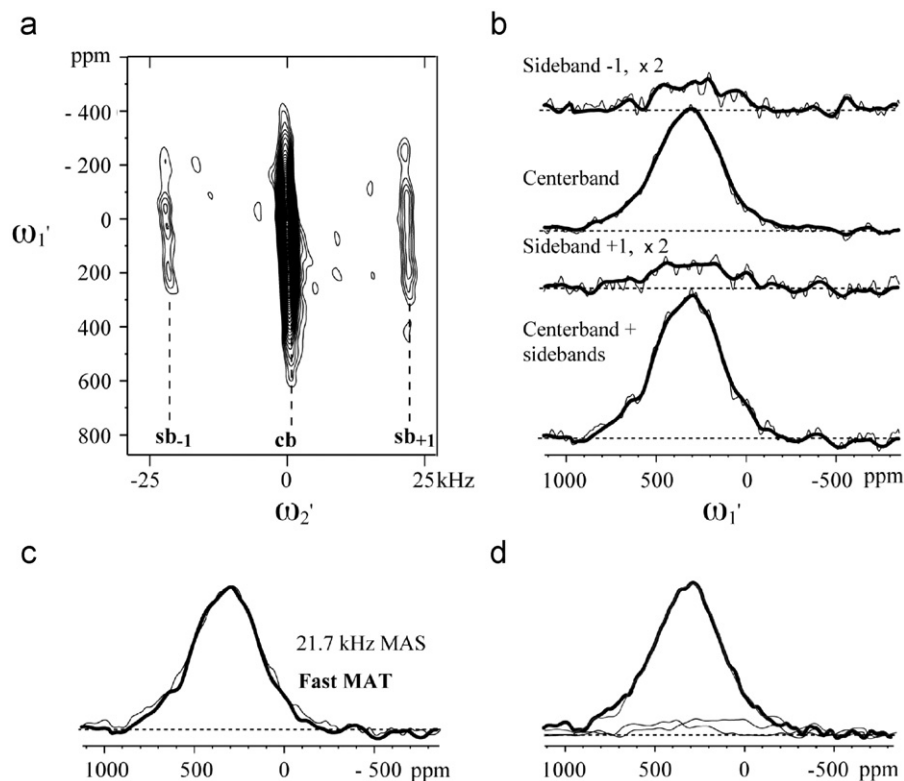

Fig 5. ^{125}Te NMR spectra of GeTe. (a) 2D fast MAT spectrum at 21.7 kHz MAS with echo-matched full Gaussian multiplication and sharing between channels after shearing. (b) Projections of sidebands and centerband from the 2D fast MAT spectra with (thick lines) and without (thin lines) echo-matched full Gaussian multiplication and sharing-between-channels after shearing. (c) Regular 21.7 kHz MAS spectrum (thin line) and isotropic spectrum of GeTe from fast MAT (sum of sidebands and centerband). (d) Quality test: comparison of the regular 21.7 kHz MAS spectrum (thick line) with the sum (thin line) of MAT center- and sideband slices in their "natural" positions; the latter are also shown individually (bands of low intensity).

3.9. Quality test

Additional shearing along ω_1, $\omega_1'' = \omega_1' + \omega_2'$, can place the sidebands along ω_1'' at their "natural" positions $\omega_{iso} + \omega_{aniso}$ as in the MAS spectrum (Fig. 4d). This enables us to experimentally deconvolute the 1D MAS spectrum into centerband and sideband contributions. Further, the sum of all signal slices should be identical to the regular 1D MAS spectrum. Thus, comparison between the regular MAS spectrum and the sum spectrum from triply-sheared fast MAT is useful for assessing the extent of spectral distortions.

The data processing using echo-matched full-Gaussian multiplication and sharing between channels after shearing was performed using the Matlab (Math Works, Natick, Massachusetts) software.

4. Results and discussion

4.1. Fast MAT on tellurides

The application of fast MAT to various tellurides demonstrates its ability of separating centerbands at the isotropic shift positions from spinning sidebands over a broad spectral range (Figs. 4 and 5a). Echo-matched full Gaussian filtering is seen to clearly improve the signal-to-noise ratio.

Thin lines in Fig. 5b show the projections of the centerband and sidebands of the 2D fast MAT spectra of GeTe, with normal Gaussian multiplication and spectral shearing, and additional three-point filtering to further reduce noise, while the thick lines represent the corresponding spectra with echo-matched full-Gaussian filtering and sharing between channels after shearing. The S/N ratio of the latter is significantly better, providing more clearly defined spectral lineshapes of centerband and sidebands. Comparison between the regular MAS spectrum and the isotropic spectrum from fast MAT of GeTe in Fig. 5c reveals that the broad line width is largely due to a wide, continuous distribution of isotropic chemical or Knight shifts. An analysis of the chemical shift anisotropy based on the ratios of centerband and sideband integrals was carried out using matNMR (version 3.9.59) [19]. The sideband manifold calculation was performed employing a gammaCOMPUTE-based algorithm combined with powder averaging. Coarse optimization was facilitated by the SIMPLEX algorithm followed by a gradient minimization to finalize the analysis. The results show that chemical sites of isotropic chemical shifts between 270 and 450 ppm have a slightly smaller $\Delta\sigma_{CSA} = 240 \pm 30$ ppm than the rest with $\Delta\sigma_{CSA} = 280 \pm 20$ ppm. With $\Delta\sigma_{CSA} < 2\omega_r$ (350 ppm for ^{125}Te), the magnitude of the first-sideband integral (< 0.1) is almost independent of the asymmetry (or biaxiality) parameter η, which can therefore not be determined reliably [20]. The quality test comparing the sum of centerband and sidebands at their "natural" positions in the triply sheared fast MAT with the regular MAS spectrum, Fig. 5d, proves that fast MAT does not produce significant spectral artifacts over a spectral range $> \gamma B_1$.

Similarly, for $Ag_{0.53}Pb_{18}Sb_{1.2}Te_{20}$, the MAT spectral quality is improved in terms of S/N ratio by use of the echo-matched full-Gaussian window function (Fig. 6a). The purely isotropic spectrum (Fig. 6b) reconstructed from centerband and sidebands with improved S/N ratio (Fig. 6a) permits more accurate quantification of the percentage of Te bonded to Sb, resonating around -1500 ppm, which accounts for 22% of the total Te. The comparison of the "infinite-speed" isotropic spectrum from fast MAT with the regular MAS spectrum in Fig. 6b sheds light on the overlap of the sidebands with the isotropic peaks. Sideband analysis reveals that Te bonded to six Pb in the bulk lattice has
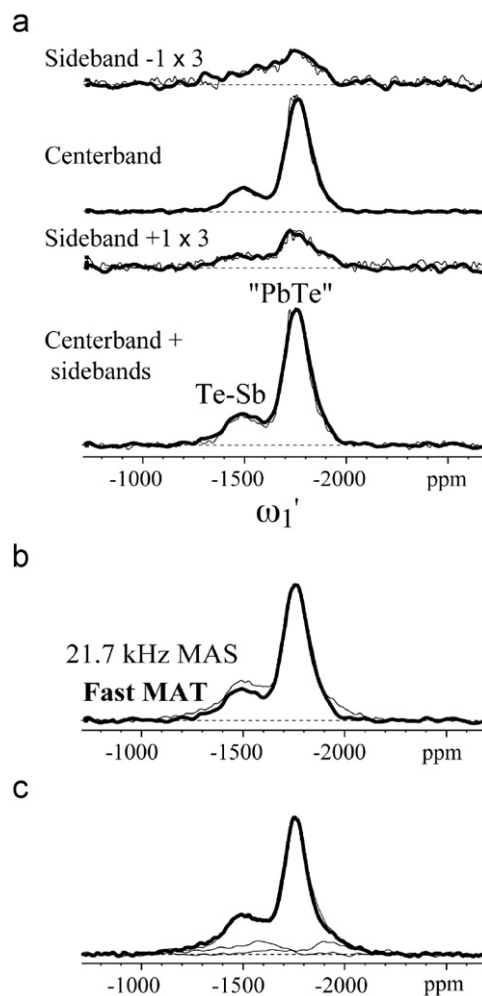

Fig. 6. ^{125}Te NMR spectra of $Ag_{0.53}Pb_{18}Sb_{1.2}Te_{20}$. (a) Projections of sidebands and centerband from the 2D fast MAT spectra with (thick lines) and without (thin lines) echo-matched full Gaussian multiplication and sharing between channels after shearing. (b) Comparison of regular 21.7 kHz MAS spectrum (thin line) and isotropic spectrum from fast MAT (sum of sidebands and centerband). (c) Quality test: comparison of the regular 21.7 kHz MAS spectrum (thick line) with the sum (thin line, barely distinguishable) of MAT center- and side-band slices in their "natural" positions; the latter are also shown individually (bands of low intensity).

a $\Delta\sigma_{CSA} = 350 \pm 20$ ppm, while Te bonded to Sb has a somewhat larger $\Delta\sigma_{CSA} = 439 \pm 15$ ppm. Similarly as in GeTe, the $\Delta\sigma_{CSA}$ of $Ag_{0.53}Pb_{18}Sb_{1.2}Te_{20}$ is comparable to ω_r so that η cannot be determined reliably. The good agreement of the sum of fast MAT centerband and sidebands in their "natural" positions with regular MAS (Fig. 6c) demonstrates that fast MAT results in no observable artifacts here.

The most dramatic difference made by the use of fast MAT for separating sidebands from centerbands over a broad range is illustrated by its application to Sb_2Te_3. The large CSA, which reflects the non-cubic, rhombohedral structure [21], combined with significant shift dispersion, makes it impossible to recognize the isotropic chemical shift pattern even at 22 kHz MAS. Fast MAT overcomes this problem, see Fig. 7. In addition, the figure shows that the centerband and sideband patterns after processing with echo-matched filtering and sharing between channels after shearing show significantly reduced noise. The intensity patterns of the sidebands, in particular those of order $+1$ and -1, suggest that at least three inequivalent Te sites are present: one corresponding to the main peak in the center, with a $\Delta\sigma_{CSA}$ of 1226 ± 30 ppm and an asymmetry parameter $\eta = 0.45 \pm 0.1$, and two shoulders with a $\Delta\sigma_{CSA}$ of 1306 ± 30 ppm and an asymmetry parameter
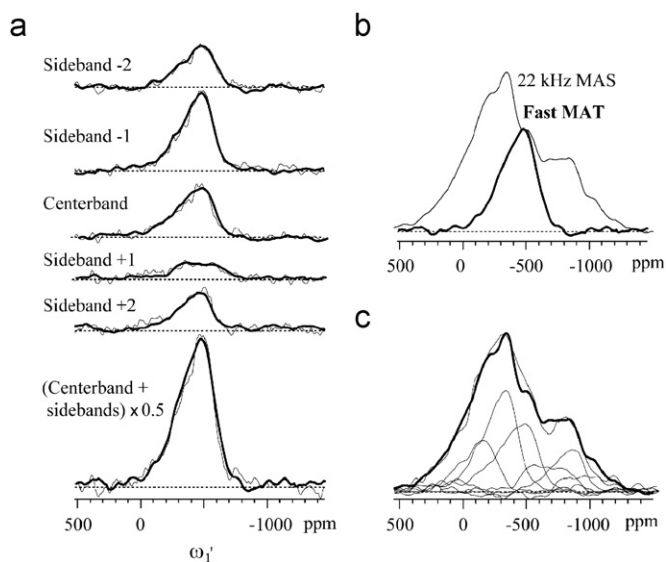
Fig. 7. ^{125}Te NMR spectra of Sb_2Te_3. (a) Projections of sidebands and centerband from the 2D fast MAT spectra with (thick lines) and without (thin lines) echo-matched full Gaussian multiplication and sharing between channels after shearing. (b) Comparison of the regular 21.7 kHz MAS spectrum (thin line) and isotropic spectrum from fast MAT (sum of sidebands and centerband). (c) Quality test: comparison of the regular 21.7 kHz MAS spectrum (thick line) with the sum (thin line) of MAT center- and side-band slices in their "natural" positions, which are also shown individually.

$\eta = 0.56 \pm 0.1$ (Fig. 7b). Fast MAT works quite well for the spectral range spanning over $\sim 1.8\gamma B_1$ as shown in the quality test comparing the regular MAS spectrum with the sum of all centerbands and sidebands in their "natural" positions of fast MAT, see Fig. 7c.

4.2. Comparison of PASS and fast MAT

Phase adjusted spinning sidebands (PASS) is a useful method for generating spectra of sidebands of order n, and after shearing, spectra with resonances only at the isotropic chemical shifts can be reconstructed. Dixon's $4 - \pi$-pulse PASS [9] was designed for lower spinning speeds, while at fast spinning, a $5 - \pi$-pulse PASS version [2,7] was implemented to avoid pulse overlap and keep the total time constant. We compare fast MAT with PASS under the same experimental conditions. In terms of minimizing pulse excitation effects, 4-pulse PASS is preferable to 5-pulse PASS. Due to relatively fast spinning and resulting short t_r in our experiments, the slight variation ($< 0.3t_r$) in total duration of 4-pulse PASS produces only negligible artifacts, smaller than an additional 180° pulse.

For moderate spectral ranges, PASS is usually preferable over fast MAT. It has a higher sensitivity and can be implemented with a small number of increments and simple data processing. The very recent development of MAT-PASS by Hung and Gan [22] using linear t_1 increments allows for even easier implementation of PASS. On the other hand, the fast MAT experiment has a significantly wider excitation range and produces fewer sideband artifacts. Fig. 8 shows the comparison of spectra of seven mixed amino acids obtained by employing different versions of PASS and fast MAT under similar conditions, compared to the undistorted spectrum from 5-pulse PASS with strong pulse excitation (2π 56.8 kHz) as a reference. With weak pulses of $\gamma B_1 = 2\pi$ 11.4 kHz, fast MAT produces only minor spectral distortions over a spectral range of ca. $1.8\gamma B_1$, while for 5-pulse PASS, the distortions are overwhelming, leaving little or no peak intensity. Even with relatively stronger pulses at $\gamma B_1 = 2\pi$ 21.9 kHz, the artifacts in the 4-pulse PASS spectrum are intolerable. Thus, PASS may
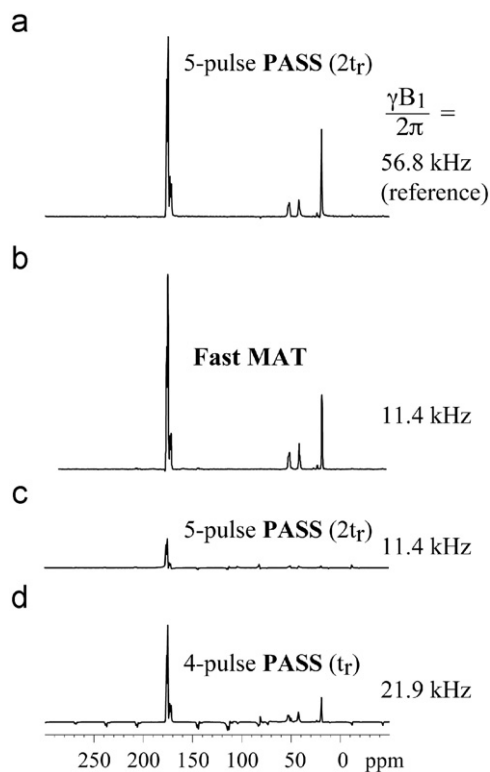

Fig. 8. Comparison of PASS and fast MAT demonstrated on a mixture of seven ^{13}C-labeled amino acids (same sample as in Fig. 3). (a) Reference five-pulse PASS spectrum obtained with strong pulses. (b) Fast MAT spectrum obtained with weak pulses, as shown in detail in Fig. 3. (c) Five-pulse PASS spectrum obtained under the same conditions as in (b). (d) Four-pulse PASS spectrum obtained with moderately strong pulses.

sometimes serve as an exploratory method, but if PASS appears to produce sideband artifacts or distortions of off-resonance signals, fast MAT can be used to generate reliable and high-quality spectra.

5. Conclusions

We have discussed several technical details of fast MAT [7]: (i) the excitation effect of the pulses on magnetization off-resonance has been analyzed numerically, and the results show a phase shift nearly linear with off-resonance frequency $\Delta\omega$ with a factor close to unity for a pair of $< 60°$ pulses and 1.26 for 90° pulses; this phase shift can be considered as resulting from precession during the pulses and thus compensated for by generating a slice with $t_{1,eff} = 0$ for 2D MAT. This approach should also be applicable to other two-dimensional experiments with chemical-shift evolution. (ii) The duration of z-periods has been minimized by cyclic decrementation, resolving issues from short rotation periods. (iii) The sensitivity was optimized by moving the maximum of the Gaussian filtering function for each t_1 value to match the echo that results from the refocusing of isotropic chemical shifts. (iv) Artifacts caused by digital rounding after shearing have been removed by the sharing-between-channels approach. Furthermore, the ^{125}Te chemical shift anisotropy parameters of various tellurium sites in tellurides have been determined by analysis of the sideband patterns at various isotropic shifts. The comparison between fast MAT and PASS has confirmed that fast MAT is more favorable for broadband excitation, with tolerable spectral distortions for wide spectra spanning up to $\sim 1.8\gamma B_1$.

Acknowledgments

References

[1] W.T. Dixon, J. Chem. Soc., Dalton Trans. 77 (1982) 3741–3748.
[2] O.N. Antzutkin, S.C. Shekar, M.H. Levitt, J. Magn. Reson. Ser. A 115 (1995) 7–19.
[3] Z.H. Gan, J. Am. Chem. Soc. 114 (1992) 8307–8309.
[4] J.Z. Hu, A.M. Orendt, D.W. Alderman, R.J. Pugmire, C.H. Ye, D.M. Grant, Solid State Nucl. Magn. Reson. 3 (1994) 181–197.
[5] J.Z. Hu, W. Wang, F. Liu, M.S. Solum, A.M. Orendt, D.W. Alderman, R.J. Pugmire, D.M. Grant, J. Magn. Reson. Ser. A 113 (1995) 210–222.
[6] Z.H. Gan, R.R. Ernst, J. Magn., Reson. Ser. A 123 (1996) 140–143.
[7] Y.Y. Hu, E.M. Levin, K. Schmidt-Rohr, J. Am. Chem. Soc. 131 (2009) 8390–8391.
[8] K. Schmidt-Rohr, Q. Chen, Nat. Mater. 7 (2008) 75–83.
[9] W.T. Dixon, J. Chem. Phys. 77 (1982) 1800–1809.
[10] F.G. Vogt, J.M. Gibson, D.J. Aurentz, K.T. Mueller, A.J. Benesi, J. Magn. Reson. 143 (2000) 153–160.
[11] E.M. Levin, B.A. Cook, K. Ahn, M.G. Kanatzidis, K. Schmidt-Rohr, Phys. Rev. B 80 (2009) 115211/1–115211/6.
[12] G. Bodenhausen, R. Freeman, D.L. Turner, J. Magn. Reson. 27 (1977) 511–514.
[13] I. Orion, J. Rocha, S. Jobic, V. Abadie, R. Brec, C. Fernandez, J.-P. Amoureux, J. Chem. Soc., Dalton Trans. 20 (1997) 3741–3748.
[14] K. Schmidt-Rohr, H.W. Spiess, Multidimensional Solid-State NMR and Polymers, Academic Press, San Diego, 1994.
[15] M. Garwood, L. DelaBarre, J. Magn. Reson. 153 (2001) 155–177.
[16] P.J. Grandinetti, J.H. Baltisberger, A. Llor, Y.K. Lee, U. Werner, M.A. Eastman, A. Pines, J. Magn. Reson. Ser. A 103 (1993) 72–81.
[17] J. Trebosc, J.P. Amoureux, Z.H. Gan, State Nucl. Magn. Reson. 31 (2007) 1–9.
[18] S.F. Liu, J.D. Mao, K. Schmidt-Rohr, J. Magn. Reson. 155 (2002) 15–28.
[19] J.D. van Beek, J. Magn. Reson. 187 (2007) 19–26.
[20] J. Herzfeld, A.E. Berger, J. Chem. Phys. 73 (1980) 6021–6029.
[21] J.L.F. Da Silva, A. Walsh, H. Lee, Phys. Rev. B 78 (2008) 224111/1–224111/10.
[22] I. Hung, Z.H. Gan, J. Magn. Reson. 204 (2010) 150–154.